Metallic Interface Induced Ionic Redistribution within Amorphous MoO₃ Films

Francesco Paparoni, Emin Mijit, Shafaq Kazim, Marco Minicucci, Nicola Pinto, Alessandro D'Elia, Salvatore Macis, Changyoung Kim, Soonsang Huh, Roberto Gunnella, Augusto Marcelli, Andrea DiCicco, and Seyed Javad Rezvani*

The phase evolution and ionic redistribution in amorphous MoO₃ films, deposited on metallic aluminium (Al) and copper (Cu) substrates and subjected to distinct thermal treatments, are systematically investigated in this work. It is shown that the metallic interface significantly modifies the formation and dynamics of oxygen vacancies within the resulted structure, reducing the oxygen content of the MoO₃ up to $x < 2.94$. The concentration of the oxygen vacancies can also be extended to the bulk via thermal treatment up to 400 °C. It is demonstrated that the MoO₃ structure on metallic substrates is affected either by the diffusion of the metallic atoms inserted from the interface, which results in a formation of the meta-stable alloy phases in case of Cu, or by the introduction of the oxygen vacancies into the crystalline matrix in case of Al. The oxygen vacancy density in the MoO₃ films with a metallic interface can be tuned via optimal choice of the metal and treatment parameters such as temperature and oxygen partial pressure. Furthermore, the intrinsic defects present in the amorphous structure enhance the ionic mobility and diffusion of the metallic ions inside the crystalline structure.

1. Introduction

The transition metal oxides with high work function and opto-electronic properties are of utmost interest in several advanced applications, such as photonics and thermochromic as well as protective coatings.[1–4] Among these materials, molybdenum oxides recently attracted the attention, due to the peculiar features of this class of oxide, originating from the interplay between the large variety of lattice configuration and the multiple valence states of Mo.[5–7] Even though MoO₃ is a high-k dielectric insulator, its electronic structure can be adjusted by modifying the oxygen substoichiometry (MoO₃₋ₓ), introducing electronic gap states that modifies the oxide's electrical conductivity.[8,9] The stoichiometric MoO₃ is an n-type material with an equilibrium concentration of defects (mainly oxygen vacancies), which cause the formation of Mo⁵⁺, that partially occupies Mo 4d band creating gap states. These states play as n-type dopant, push the MoO₃ Fermi level closer to the conduction band. A continuous removal of oxygen may reduce MoO₃ to MoO₂, the lowest stable molybdenum oxide, which contains Mo⁴⁺ cations, that give rise to a partially filled 4d band resulting in semi-metallic states.

The consequent electronic properties of the vacancy formation have shown applicability across a number of technological fields, including promising electrochromic, battery cathode material, and gas sensors.[10,11] It has also been shown that

F. Paparoni, E. Mijit, S. Kazim, M. Minicucci, N. Pinto, R. Gunnella, A. DiCicco, S. J. Rezvani
Sez. Fisica, Scuola di Scienze e Tecnologie
Universitá di Camerino
via Madonna delle Carceri 9, Camerino 62032, Italy
E-mail: seyedjavad.rezvani@unicam.it

A. D'Elia
CNR - Istituto Struttura della Materia and Elettra-Sincrotrone Trieste
Basovizza Area Science Park, Trieste 34149, Italy

S. Macis
Dipartimento di Fisica
Universitá di Roma "la Sapienza"
Piazzale Aldo Moro 5, Roma 00185, Italy

C. Kim, S. Huh
Center for Correlated Electron Systems
Institute for Basic Science
Gwanak-ro, Gwanak-gu, Seoul 08826, Korea

C. Kim, S. Huh
Department of Physics and Astronomy
Seoul National University
Gwanak-ro, Gwanak-gu, Seoul 08826, Korea

A. Marcelli, S. J. Rezvani
INFN- Laboratori Nazionali di Frascati
Via Enrico Fermi 54, Frascati 00044, Italy

A. Marcelli
RICMASS – Rome International Center for Materials Science Superstripes
Via dei Sabelli 119A, Roma 00185, Italy

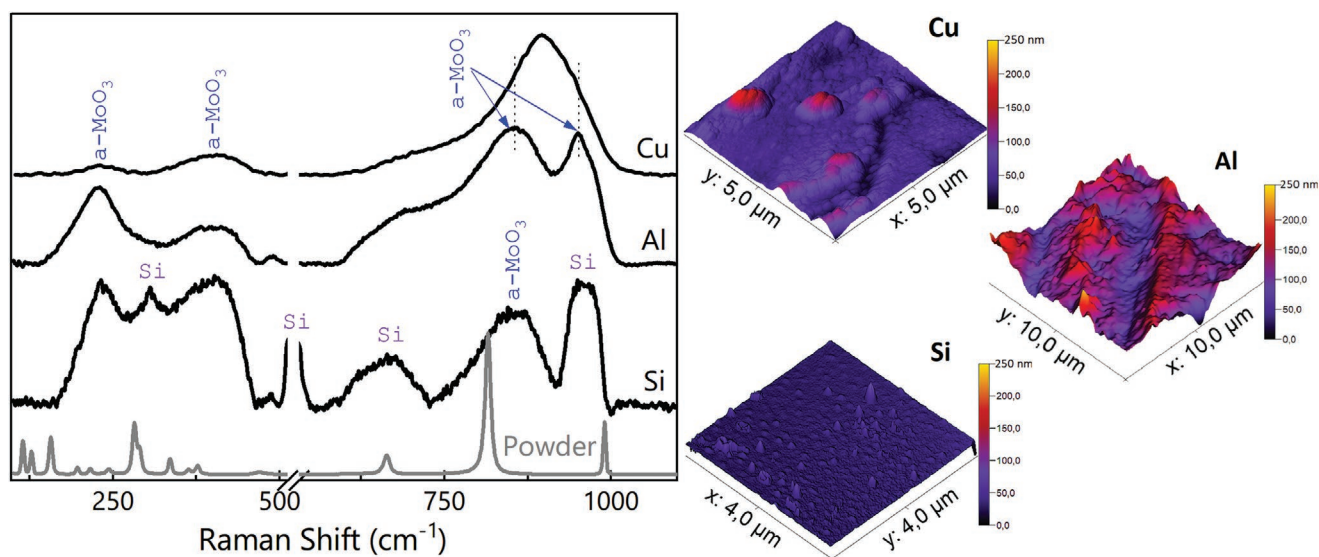**Figure 1.** Raman spectra (left) and AFM images (right) of 300 nm of MoO_3 film on three substrate materials. The amorphous MoO_3 (α-MoO_3) peak positions are highlighted and compared with the spectra of the bulk MoO_3 powder used for the deposition.

the thin film oxides on metallic substrate exhibit an enhanced catalytic activity compared to their bulk counterparts, probably due to the charge-transfer interactions between the metal substrate and the oxide layer on the nanometer length scale.[12] The high work function and hole transport properties of MoO_{3-x}/Cu system has been also investigated to improve the conversion efficiency of the cell using the doping effect of Cu.[13–15] On the other hand, recent works suggest that coating the inner part of radio frequency cavities with high work function Mo oxides can significantly improve the performance of such devices under intense electric fields.[16] A thin layer of MoO_3 on a copper substrate could decrease the roughness of the surface, reducing the presence of tips and defects (i.e., the rate of breakdown phenomena) while increasing the discharge resistance in high electric field due to its high work function.[17] It has been demonstrated that the conductivity can increase in a thin MoO_3 film deposited over a metallic substrate, while the bulk work function remains high.[18] This effect occurs in the first few layers from the interface up to 10 nm. This interfacial interaction usually leads to the reduction of Mo oxide, generating oxygen vacancies and defects, as well as doping effect via metallic element diffusion into the oxide crystalline structure. It has been suggested by Greiner et al., that this exchange can strongly depend on the oxide formation enthalpy and the difference between chemical potentials of the film and the substrate.[18] Such exchange can also depend on physical and ambiental parameters, such as film thickness, temperature, and oxygen partial pressure.[14,19,20] However, a deep understanding of the interaction mechanism and subsequent control over the defect concentration (e.g., oxygen vacancy) is still missing.

In this work, the role of metallic substrates on the ionic redistribution in thin amorphous MoO_3 films has been investigated. The results were compared with those on non-metallic substrates as a function of various environmental parameters. The diffusion of metallic ions into the MoO_3 lattice and the enhancement of the oxygen vacancies induced by the metallic interface is discussed. These results bring us closer to a better understanding of the interfacial interaction mechanism and open the possibility to control the oxide stoichiometry as well as the concentration of oxygen vacancies that can be exploited in novel applications.

2. Results

2.1. As Deposited (AD) Films

The morphological analysis of the as deposited samples are shown in **Figure 1**. Results show a uniform distribution of the film on all substrates. The roughness of the substrates were measured to be $\approx$23, 37, and 4 nm for copper, aluminum, and silicon, respectively. The deposition of the film slightly decreases the roughness of the sample, with values of $\approx$ 21, 30, and 3 nm for the as deposited films on copper, aluminum, and silicon substrates, respectively. The homogeneity of the films was studied collecting energy dispersive spectroscopy maps (see Supporting Information) which indicate the uniform distribution of the molybdenum and oxygen content through the samples. Furthermore, the samples were characterized by X-ray fluorescence measurements, to identify possible contamination which was not detected (see Supporting Information). The structural analysis performed with the Raman spectroscopy on the as deposited samples shows the formation of amorphous molybdenum oxide structures on all samples (see Figure 1). Spectra show broadened features in all samples at 230, 405 and 710 cm^{-1}. The first two components can be assigned to vibrational excitation of Mo^{5+} and oxygen bonds in amorphous MoO_3,[16,21] while the component at 710 cm^{-1} can be assigned to the B_{3g}-ν(OMo_3) of the amorphous MoO_3.[22] At higher wave numbers, the copper samples show a significant difference compared with the films on the other two substrates. The silicon and aluminum samples show two main components
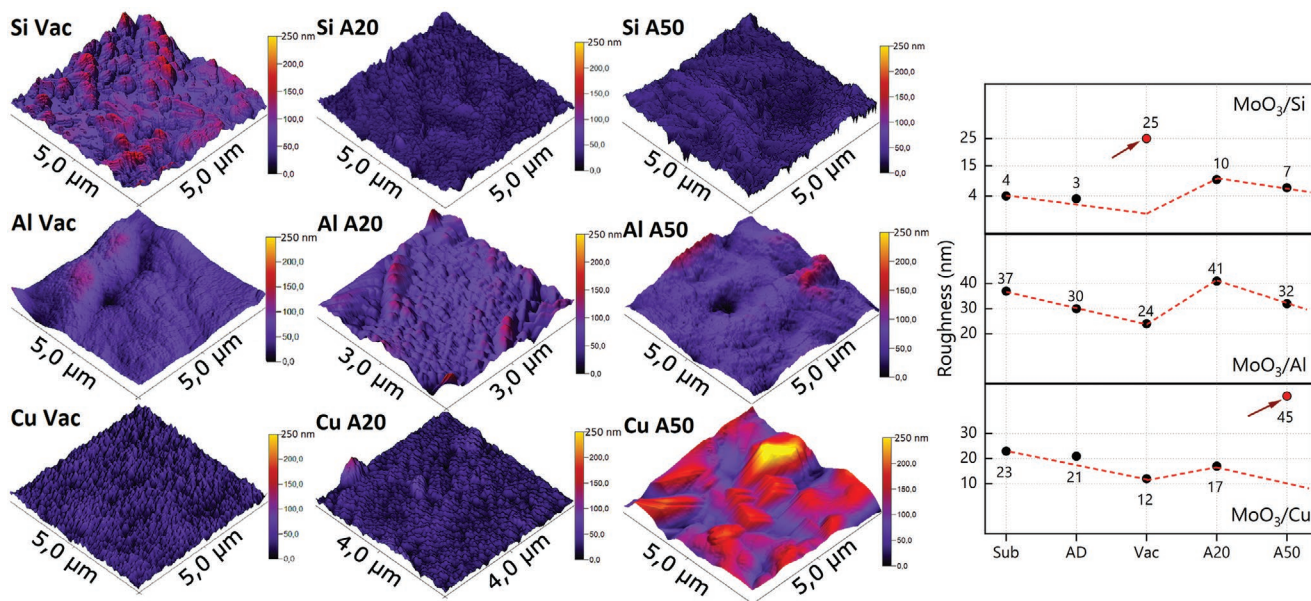
**ADVANCED
SCIENCE NEWS**

www.advancedsciencenews.com

**ADVANCED
MATERIALS
INTERFACES**

www.advmatinterfaces.de

Figure 2. AFM images of MoO$_3$ films on silicon (Si) aluminum (Al), and copper (Cu) after the thermal treatment in vacuum (Vac), 20 mbar (A20), and 50 mbar (A50) of air partial pressure (left). The corresponding average roughness values, together with the results obtained from the substrates (Sub) and of the as deposited films (AD) (right). Samples show a similar trend in roughness variation based on the treatments, with two exceptions evidenced by arrows: the abrupt increase of roughness of Si annealed in vacuum and copper annealed in 50 mbar air partial pressure. The abrupt increase is attributed to the formation of Mo$_4$O$_{11}$ and copper oxide, respectively. The red dashed line is a guide for eyes.

at 853 and 951 cm^{-1}, while the film on copper shows a single broad component at 898 cm^{-1}. The two features observed on the former substrates can be assigned to the asymmetric stretching modes of MoO$_3$: B$_{1g}$-ν(OMo$_2$) and B$_{1g}$-ν(Mo=O).[22] The attempt to fit the single broad feature of the film on copper substrate reveals the presence of the two aforementioned components observed on Si and Al as well as the presence of a third component centered at 898 cm^{-1} (see Supporting Information). The latter can be assigned to the formation of Cu–Mo–O kind alloys[18,23] resulted from the film/metal interface interactions.

2.2. Annealing in Vacuum

Morphological analysis of these samples reveal a slight decrease of the roughness in copper and aluminum samples and an increase in silicon samples, with formation of 3D islands (see **Figures 2** and **3**A). The formation of these structures is due to Mo sub-oxides persistence that will be discussed later. The film on copper shows a granular structure with grains in the range 70–100 nm (see Figures 2 and 3G), while the one on aluminum present a uniform distribution without dominant grains (see Figures 2 and 3D). The structural analysis shows significant changes in the Raman spectra, compared with the as deposited ones (see **Figure 4**a). The formation of the metallic MoO$_2$, which is identified via eleven Raman active modes (see **Table 1**), is evident. The downward shifted peak at ≈127 cm^{-1}, can also be associated to a rigid chain mode (RCM) of an intermediate oxidation state MoO$_{3-x}$.[24] On copper and silicon substrates, on the other hand, there are relatively weak components at 790, 812, 834, 845, 906, and 915 cm^{-1}, that are signatures of the formation of metastable Mo sub-oxides. These features have

been identified as Mo$_4$O$_{11}$ on silicon and Cu–Mo–O alloy on copper.[25,26]

The reduction of MoO$_3$ upon vacuum treatment is a well known effect,[27,28] that occurs due to the loss of oxygen from the structural lattice of the MoO$_3$. The formation of the metastable phase Mo$_4$O$_{11}$ is usually expected as the intermediate step in the reduction of MoO$_3$ to MoO$_2$.[29] The persistence of the intermediate Mo$_4$O$_{11}$ sub-oxide might also explain the presence of 3D islands on the silicon substrate. The large volume of Mo$_4$O$_{11}$ can result in an extensive volumetric expansion causing the disruption of the uniform film formation.[30] The absence of the intermediate phases on aluminum substrate is a result of metal assisted reduction of the film, forming MoO$_2$ via oxidation of the metallic substrate (3MoO$_3$ + 2Al → 3MoO$_2$ + Al$_2$O$_3$). The one step reduction of MoO$_3$ to MoO$_2$ in copper substrates is also accelerated by Cu diffusion into the film. These ions act as n-type dopants, and increase the number of oxygen vacancies via alloy formation,[13] recognized by two active modes at 812 and 915 cm^{-1} (see Figure 4a).

2.3. Annealing in 20 mbar of Air

The films on silicon shows a homogeneous growth with some slabs of the molybdenum oxide layers (see Figure 3B). This sample shows a higher roughness (10 nm) compared with the as deposited case. On the other hand, the film synthesized on aluminum (Figures 2 and 3E) shows a granular-like structure (grain size 100–150 nm), on which patches of the layered structure are also present. The roughness of the sample is higher compared to the vacuum annealed case (≈41 nm). The film on copper shows a structure similar to the vacuum case, with a
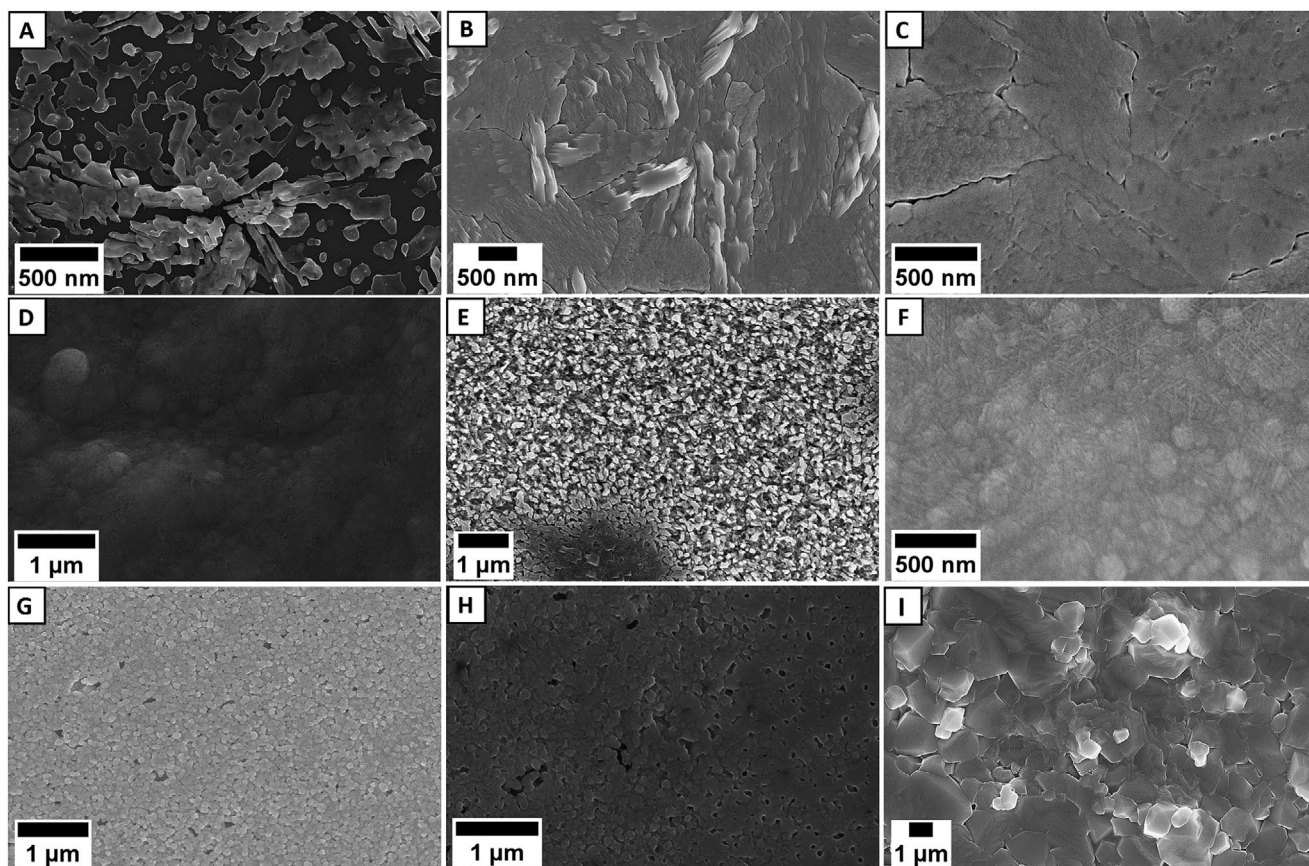
**ADVANCED
SCIENCE NEWS**

www.advancedsciencenews.com

**ADVANCED
MATERIALS
INTERFACES**

www.advmatinterfaces.de

Figure 3. SEM images of MoO$_3$ films on A–C) silicon, D–F) aluminum, and G–I) copper after annealing in vacuum (left column), 20 mbar air (central), and 50 mbar air (right).

granular structure with grain size in the range 70–80 nm (see Figures 2 and 3H), with a bluish-green appearance (see Supporting Information) and with a relative roughness of ≈17 nm.

The structural analysis of the samples annealed in 20 mbar air partial pressure are shown in Figure 4b. Films synthesized on silicon and aluminum show the transition to the crystalline α-MoO$_3$[24] (see Table 1). Looking at the lower wavenumber region, the film on silicon shows relatively similar spectrum compared with the one taken from the MoO$_3$ powder before the deposition (see Figure 1). However, the spectrum of the sample

on aluminum shows the inversion of the excitation modes at 118 and 130 cm^{-1} as well as 284 and 292 cm^{-1}. It has been suggested[19,32] that the intensity ratio of the former components can be correlated to the dimension of the crystallites formed within the films. In our case the ratio I$_{130}$/I$_{118}$ has been changed from 0.75 to 1.43, which suggests the formation of larger crystallites in film on aluminum compared with the ones formed on silicon substrate, in agreement with the morphological analysis. On the other hand, since the latter two modes are polarized in the same direction (parallel to c-axis) while belonging to
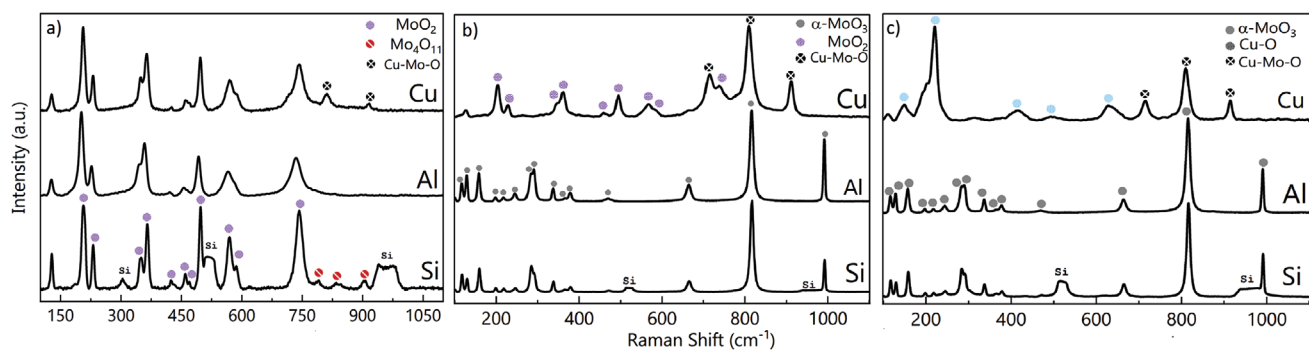

Figure 4. Raman spectra of the annealed samples a) in vacuum, b) 20 mbar of air, and c) 50 mbar of air partial pressure. Every graph confronts the spectra of the films on copper (Cu), aluminum (Al), and silicon (Si). The silicon's peak at 521 cm^{-1} has been removed to improve visualization.

2200453 (4 of 10)

Table 1. Fitted peak centers of the Raman spectra acquired from the film on aluminum (Al), copper (Cu), and silicon (Si) substrates after thermal treatment (vac, A20, A50). MoO_2 and MoO_3 modes with no specified reference are in agreement with Chamacho-López et al.,[24] while copper oxide modes have been assigned from Solache-Carranco et al.[31] The shifted modes related to the copper diffusion into the MoO_3 matrix are marked (*).

Si vacuum	Si A20	Si A50	Al vacuum	Al A20	Al A50	Cu vacuum	Cu A20	Cu A50	Assignments
								110	Γ_{12}
	118	117		117	116				B_{2g} RCM[32]
127	130	129	127	129	128	128	127		B_{3g} RCM[32]
								148	$\Gamma_{15}^{(1)}$ [33]
	159	159		158	157				A_g-$\delta(O_2Mo_2)_n$
	199	198		198	197				B_{2g}-$\tau(Mo{=}O)$[32]
205			202			206	203	202	A_g-$\delta(OMo_2)$
	219	218		218	217				A_g-$\delta(OMo_2)$
								221	$2\Gamma_{12}$
230			227			230	228		A_g-$\delta(OMo_2)$
	245	245		245	244				B_{3g}-$\tau(Mo{=}O)$[32]
	284	284		283	284				B_{2g}-$\delta(O{=}Mo)$
	292	292		291	291				B_{3g}-$\delta(O{=}Mo)$
								315	A_g (CuO)[34]
349	338	338	345	337	337	349	348		A_g-$\delta(OMo_3)$
364	366	366	359	366	365	364	362		A_g-$\delta(O{=}Mo)$
	379	379		378	378				B_{1g}-$\delta(O{=}Mo)$[32]
								414	$2\Gamma_{15}^{(1)}$
422			421			425			A_g-$\delta(O{=}Mo)$
459			455			460	460		A_g-$\delta(O{=}Mo)$
467	471	471	464	470	469	469	466		B_{1g}-$\nu(OMo_3)$
496			492			497	495		m-MoO_2
								500	Γ_{25}
569			566			570	565		m-MoO_2
588			583			589	582		m-MoO_2, B_{1g}-$\nu(Mo{-}O)$
							637	633	$\Gamma_{15}^{(2)}$
	665	665		664	664		715*	715*	B_{3g}-$\nu(OMo_3)$
743		735				742	738		m-MoO_2, B_{2g}-$\nu(Mo{-}O)$
790, 834, 845									Mo-O (Mo_4O_{11})[25]
	817	816		817	816	812*	810*	810*	B_{1g}-$\nu(OMo_2)$
906									O-Mo-O (Mo_4O_{11})[25]
	992	992		991	991	915*	912*	914*	B_{1g}-$\nu(O{=}Mo)$

different symmetry groups, their intensity ratio is suggested to be correlated to the distortions on the c-axis generated by the O vacancies and, therefore, can be used as an indicator of the stoichiometry of the films.[19] The inversion observed in the spectra on aluminum compared with the one on silicon ($I_{284}/I_{292} = 1.46$ on Si and 0.79 on Al) suggests presence of defective oxygen vacancies within the film. Our analysis estimates the O/Mo ratio to be ≈2.945 for aluminum and ≈2.953 for silicon.

The film on copper substrate reveals a mixture of MoO_2 (with components at 203, 228, 348, 362, 460, 466, 495, 565, 582, and 738 cm^{-1}) with a sub-oxide phase similar to that observed on sample annealed in vacuum (with components at 127, 715, 810, and 912 cm^{-1}). These shifted peaks can be assigned to a distorted α-MoO_3 phase with the elongated O$-$Mo$_2$ and O$=$Mo bonds, and shortened O$-$Mo$_3$. The copper insertion is also identified from the symmetric stretching vibrations of MoO_4 tetrahedra in the as deposited film on copper substrates.[18,23] This effect has been also observed in a codeposition of Cu$-$O and MoO_3, which resulted in a shift of the B_{1g}-$\nu(OMo_2)$ stretching mode as well as B_{1g}-$\nu(O{=}Mo)$ to lower wavenumbers, depending on the copper oxide content within the films.[26] Our results are in good agreement with the shift observed by Sundeep et. al.,[26] with a similar weak component around 637 cm^{-1}, assigned to the Cu$-$O B_g Raman active mode. The vibrational B_{3g}-$\nu(OMo_3)$ mode was not observed in the previous study, while its shift from 665 to 715 cm^{-1} can be

**ADVANCED
SCIENCE NEWS**

www.advancedsciencenews.com

**ADVANCED
MATERIALS
INTERFACES**

www.advmatinterfaces.de

expected from the distortion related to the Cu insertion into the crystalline structure.

2.4. Annealing in 50 mbar of Air

In higher air partial pressure, the film on silicon shows a similar morphology and roughness (≈7 nm) compared to films treated at lower air partial pressure (see Figures 2 and 3C). The film on aluminum shows a smooth surface with a moderately lower roughness (≈32 nm) with respect to the lower partial pressure treatment (Figures 2 and 3F). On the other hand, the film on copper presents a uniform structure, with large planar grains in the range 200–500 nm with the clear formation of slabs (see Figures 2 and 3I). The roughness in this case is increased to a nominative value of ≈45 nm due to formation of the copper oxides.

The structural analysis of the samples shows transitions to the α-MoO_3 phase in films on silicon and aluminum substrates. However, the film on aluminum shows a reduced oxygen vacancy concentration with respect to the annealing in 20 mbar of air. The reversion of the excitation modes in aluminum substrate is still present, with an intensity ratio of 1.15 for the RCM modes and 0.91 for the ratio between the B_{2g} and B_{3g}-δ(O=Mo) modes. This slight decrease of the RCM ratio, with respect to the annealing in 20 mbar of air, suggests the formation of similar crystallite sizes on the two substrate materials, while the higher ratio of the latter modes in the film deposited on the aluminum substrate indicate a decrease of the oxygen vacancy density by reoxidation. Conversely, in films on copper substrates, the structure is significantly altered. While the stretching modes of MoO_3 are shifted in a similar way to the previous annealing mode, the MoO_2 components are interchanged with the components that can be attributed to the formation of copper oxides at 110, 148, 221, 315, 414, 500, and 633 cm^{-1}. The higher oxygen partial pressure results in the oxidation of a portion of the copper ions diffused into the MoO_{3-x} lattice. The oxide formation is evidenced by high intensity of the peak at 221 cm^{-1}. The abrupt increase of the sample roughness can also be correlated to the formation of the copper oxide with a larger volume compared with the monoclinic MoO_2.

3. Discussions

The reduction process is usually expected to start with the removal of oxygen ions close to the surface and to the creation of isolated oxygen vacancies, with electrons being localized on an adjacent Mo^{6+} ion. This process results[35] in the formation of two Mo^{5+} or a double reduced Mo^{4+}. With the increase of the O vacancy concentration, strings of edge-sharing MoO_6 octahedra are created from the original corner-sharing octahedra present in the stoichiometric MoO_3.[36] The vacancies diffuse relatively slowly inside the bulk, depending on the annealing temperature.[37] Due to the difference in the work functions between MoO_3 and its sub-oxides, the electron transfer to MoO_3 surface occurs via an autocatalytic reaction across the MoO_2/MoO_3 interface. This will result in the formation of an accumulation layer, that is an excess of negative charges at the MoO_3 surface which result in the downward bending of the energy bands at the surface. With the lower edge of the conduction band, shifted below the Fermi level, the extra electrons from MoO_2 will populate the low-laying levels within this band. Since MoO_3 is a d^0 oxide, the lower part of its conduction band consists of antibonding Mo–O orbitals of mainly Mo 4d character. The population of such orbitals results in the decrease of the bond energy. It becomes, therefore, easier to break the Mo–O bond, releasing oxygen from the surface. The oxygen anions released during this process diffuse in gas phase, but can be recaptured by the topotactically formed MoO_2 domains, which consequently re-oxidize to Mo_4O_{11}. An abrupt increase of the crystal lattice mobility of MoO_3 (and molybdates) at high temperatures (e.g., 400 °C) results in the depletion of MoO_3, which acts as the oxygen source of the process and, hence, the accumulated Mo_4O_{11} gradÎually reduces to MoO_2.[38]

Our results, suggest that the formation of O vacancies at the metal/metal-oxide interface speeds up the depletion of oxygen and formation of MoO_2. Hence, the presence of the intermediate product Mo_4O_{11} is hindered on metallic substrates with respect to the non metallic case. The bulk oxygen vacancy density and redistribution can be significantly modified via the metal–metal oxide interface. In **Figure 5**, the oxygen/molybdenum ratio is plotted as a function of the ratio of the intensity of B_{2g} and B_{3g}-δ(O=Mo) modes for different substrates and thermal treatments. From the Raman intensity ratio of our samples, using a linear fit based on the results of the annealing at different conditions of bulk MoO_3 reported by M. Dieterle et al.,[19] the oxygen concentration in our samples could be calculated. In Figure 5a our results (in red) are compared with the results of Castro Silva et al.,[32] from the annealing of MoO_3 at 400 °C in O_2 atmosphere (in blue), as well as the results of commercial MoO_3 annealed at different temperature ad oxygen partial pressure, reported by Dieterle et al.[19] (in black).

The role of oxygen abundance in the annealing process, reducing the vacancies concentration, as well as metallic interface effect, with the opposite result, is evident in Figure 5. The increase of the oxygen content via the increase of the air partial pressure leads to an almost identical stoichiometry, on the silicon substrate, with respect to the MoO_3 powder used for the deposition ($x = 2.958$ for the latter and $x = 2.957$ the former). Our results on silicon substrates are in agreement with a linear dependence of the oxygen sub-stoichiometry with the oxygen partial pressure and annealing temperature, as compared with the results of refs. [19,32] that indicate a range of the x from $2.952 < x < 2.962$ in MoO_{3-x} self-standing samples, annealed at high temperature and in various air partial pressure. However, our results on aluminum substrate present a more evident reduction of the oxygen content, with a decrease of the O/Mo ratio in the film respect to the bulk powder of ≈0.5% for "A20" and 0.4% for the annealing in 50 mbar partial pressure ("A50"). This confirms that the redox process is facilitated by the metal substrate at the metal-oxide interface. As suggested by Greiner et al.,[18] the formation of oxygen vacancies at the interface can be correlated to the difference between the metal and the oxide's oxidation potential. Given the lower enthalpy of formation of aluminum oxide respect to silicon oxide, the oxidation of the metallic substrate act as a fuel of the reduction
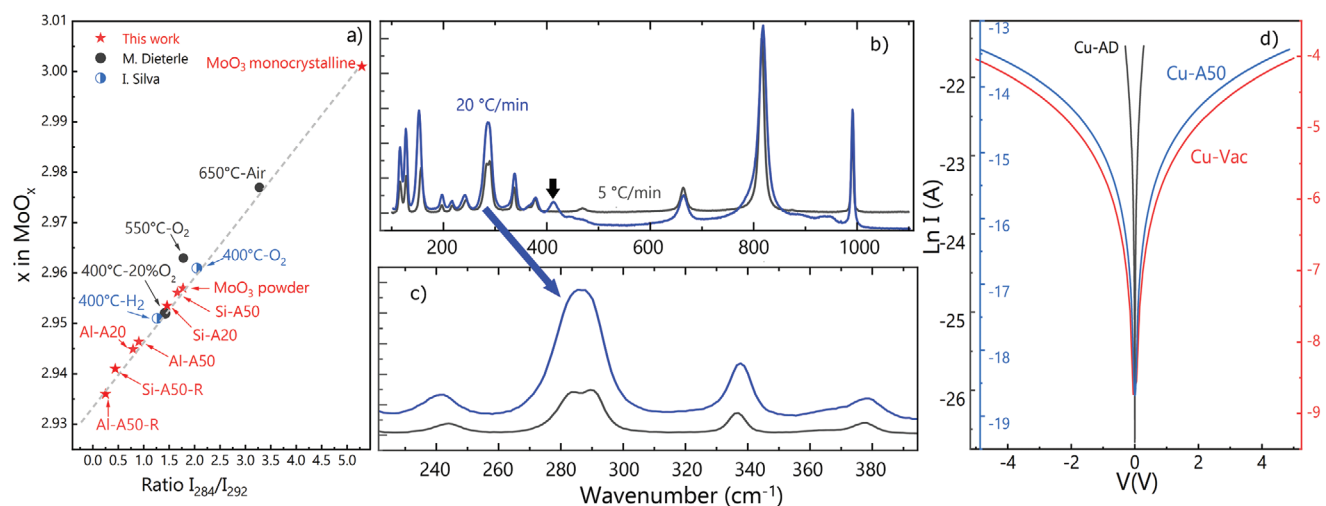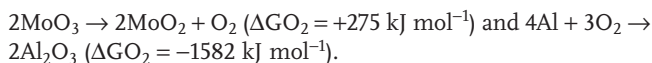
**ADVANCED
SCIENCE NEWS**

www.advancedsciencenews.com

**ADVANCED
MATERIALS
INTERFACES**

www.advmatinterfaces.de

Figure 5. a) Sample stoichiometry as a function of the intensity ratio of the B_{2g} and B_{3g}-δ(O=Mo) modes of MoO_3. The x of our samples and the intensity ratio of the results of de Castro Silva et al.[32] (in blue) have been calculated from the equation of the linear trend reported by Dieterle et al.[19] (in black). In red, points related to our films on Al, Si, MoO_3 bulk powder and the MoO_3 monocrystalline flake. The ratio calculated from the samples subjected to rapid annealing (20 °C min^{-1}) are also reported and labeled Si, Al "A50-R". b) Films on aluminum substrate subjected to annealing in 50 mbar of air partial pressure and different annealing rates. c) Inset showing the evolution of the B_{3g}-δ mode in the rapid annealing case. d) Room temperature I–V characteristic of as deposited (AD) MoO_3 films and after thermal treatment in vacuum and 50 mbar air partial pressure on copper substrates.

$2MoO_2 \rightarrow 2MoO_2 + O_2$ ($\Delta GO_2 = +275$ kJ mol^{-1}) and $4Al + 3O_2 \rightarrow 2Al_2O_3$ ($\Delta GO_2 = -1582$ kJ mol^{-1}).

We observed that the dynamics of the oxygen rearrangement also plays an important role in the final vacancies distribution in the films. A similar film deposited on the aluminum substrate and subjected to a rapid thermal annealing (20 °C min^{-1} in 50 mbar air partial pressure) points to a significantly larger vacancy density, that is observable from the overlap of the two components at 284 and 292 cm^{-1} as well its shift to lower wavenumber (see Figure 5b). While in this case there is no possibility to calculate the ratio of the oxygen content, it is suggested that in such cases the x should be lower than 2.94.[25] Furthermore, the broadening of the major scattering components as well as broad background observed in the rapid annealing, indicates the destruction of the translational symmetry via removal of oxygen from the MoO_3 and the combination of the acoustic and optical mode, confirming a defective structure.[39] The dynamic of the oxygen rearrangement, being a slow reaction,[37] was also confirmed in another sample on silicon substrate subjected to an identical rapid annealing and is identified as Si-A50-R with $x = 2.941$ (see Figure 5).

On the other hand, the films on copper substrate show the alloy formation within the MoO_3 film. Copper is known to replace O atoms within the crystalline matrix, forming copper molybdates.[40–42] The alloy formation can be associated with Cu_yMoO_3 quasi-ternary system as suggested in previous studies[43] that results in formation of Mo^{5+} and is accompanied by formation of the MoO_2 sub-oxidation. The increase of the oxygen partial pressure results in re-oxidation of the MoO_2 sub-oxide as well as diffusion of the oxygen to the substrate and oxidation of the copper while the saturated ternary phase remains persistent. However, the exact dynamics and phase transformation specially the diffusion of the oxygen within the lattice requires further studies.

Alloy formation and oxygen vacancy creation both contribute to the reduction of the work function on copper substrate as previously observed in refs. [18,43], with the saturation of the work function to values around 6 eV, particularly in regions close to the interface (see also the Supporting Information). Our results demonstrate that the oxygen vacancy and alloy formation can be extended to the bulk structure with a suitable annealing process. This process is also expected to significantly alter the electronic properties of the final films. Resistivity measurements of the films deposited on copper substrate shows significant variation based on the annealing process (i.e., the reduction of MoO_3 and the concentration of Cu atoms in the bulk), as shown in Figure 5d. The as deposited samples exhibit a high resistance (3×10^{11} Ωcm) as expected for an amorphous MoO_3 film. The sample annealed in vacuum shows a significant decrease of the resistivity, with a value of 7×10^4 Ωcm, in agreement with the formation of semi-metallic MoO_2. Both values are in good agreement with the results reported by Miyata et al.[44] On the other hand, the film annealed in 50 mbar air partial pressure shows a moderate decrease in the resistivity to a value of 5×10^9 Ωcm. This values is too high to be attributed to the copper oxide resistivity[45] (both Cu_2O and CuO) and point to a possible partial copper atom insertion into the metal oxide and formation of the alloy. The large crack density formed due to the lower thermalization of samples on silicon and aluminum, rendered the attempts to investigate the resistivity on these samples unreliable. A very slower annealing rate is expected to reduce the crack formations.

The results found on the metallic substrates raise the question whether the ionic redistribution is triggered by the structural defects present in the as deposited films or are induced by the metal–metal oxide interface. In order to investigate the structural evolution, in situ Raman measurements were carried out on a film deposited on the copper substrate as
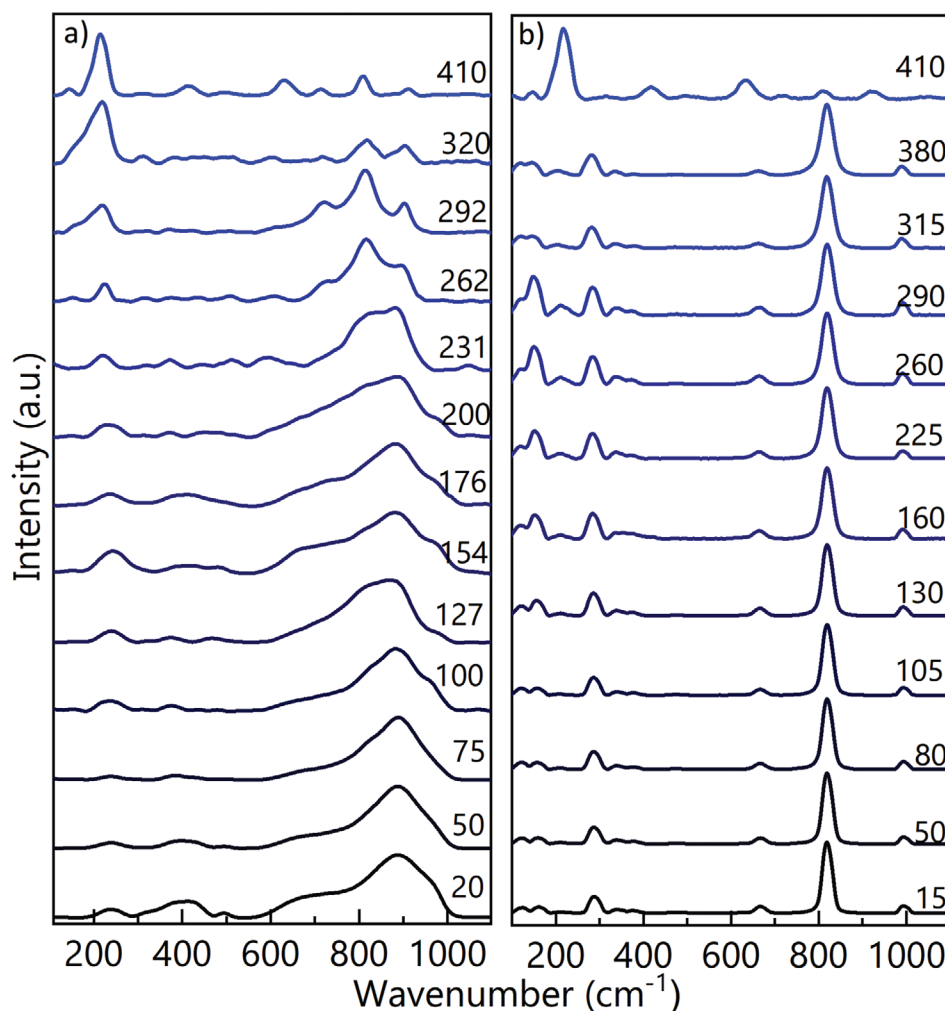
**ADVANCED
SCIENCE NEWS**
www.advancedsciencenews.com

**ADVANCED
MATERIALS
INTERFACES**
www.advmatinterfaces.de

Figure 6. In situ Raman spectroscopy during thermal treatment in 50 mbar of air partial pressure. a) 300 nm of MoO_3 film on copper, b) monocrystalline MoO_3 flake on copper. On the right side of the spectra, the numbers indicate the temperature of the samples (in °C) during the acquisition.

well as a monocrystalline MoO_3 flake, exfoliated and deposited on copper substrate (see Supporting Information). As shown in **Figure 6**a, the as deposited film shows an identical amorphous structure similar to the previous set, with the principal component at 898 cm^{-1}. As the temperature increases, a broadening of the main component of the amorphous structure is observed up to 200 °C. The main crystalline component at 814 cm^{-1} appears with further increase of the temperature over 260 °C. At higher temperatures, the splitting of the broad peak into three components at 714, 810, and 914 cm^{-1} is observed. The Cu–O active mode is also clearly observable at the same temperature range of the splitting of the three vibrational components of the metal alloy oxide, as well as downward shift of the B_{1g}-$\nu(OMo_2)$. While the active component at 405 cm^{-1} is hindered by the increase of the temperature, new features probably due to intermediate oxidation states occur. By increasing the temperature, the active mode observed at 230 cm^{-1} undergoes a continuous shift to the final value of the intense peak at 220 cm^{-1}, expected from the formation of the copper oxide.

On the other hand, the flake at room temperature exhibits the typical crystalline MoO_3 spectrum, as expected from a monocrystalline sample (see Figure 6b). During the annealing process, no significant modifications of the spectrum are observed. Over 160 °C, while the formation of copper oxide (shoulder around 220 cm^{-1}) starts to appear, a minor downward shift (from ≈288 to 284 cm^{-1}) of the B_{3g}-$\delta(O{=}Mo)$ occurs, probably due to the inversion of the intensity of the modes associated to the formation of oxygen vacancies during the oxidation–reduction process at the interface. The variation of the intensity of the peak centered around 159 cm^{-1} could also be related to the formation of copper oxide and the presence of intermediate oxidation states due to oxygen loss. Finally, over 400 °C the intensity of MoO_3 modes drops, highlighting Cu_2O vibrational modes. At the same time, similar to the annealing of the film, MoO_3 stretching modes (665, 817, and 993 cm^{-1}) suddenly shift to 716, 811, and 922 cm^{-1}. These results confirm that the formation of the Cu–Mo–O alloy occurs by the diffusion of Cu atoms inside the film as a function of temperature, though the presence of intrinsic defects enhances the gradual insertion of Cu inside the structure.

**ADVANCED
SCIENCE NEWS**

www.advancedsciencenews.com

**ADVANCED
MATERIALS
INTERFACES**

www.advmatinterfaces.de

4. Conclusions

In present work, the ionic redistribution in the amorphous metal oxide film (MoO_3) at metallic interface, via thermal treatment, was investigated and compared with non metallic substrates. Our results indicate that the formation of the oxygen vacancies is significantly enhanced at the metallic interface and can be extended to the bulk via thermal treatment. The oxygen vacancy density resulting from the partial occupation of the 4d band of the MoO_3 due to ionic interchange at the metal–metal oxide interface can be modulated via the annealing parameters. The metal/metal-oxide interphase formation leads to significant modifications of the electronic properties of the final structure, as confirmed by resistivity measurements. Our results also evidence that the presence of intrinsic defects within the initial structure enhances the ionic redistribution and diffusion within the crystalline lattice. Finally, the morphological analysis shows modifications of the average film roughness, subjected to thermal treatments, that could be optimized for several advanced applications. These results open new perspective about the employment of the metal/metal-oxide interface in various applications, such as the RF cavity protective coatings, that demands for high work function and low resistivity materials, as well as in organic electronics for the formation of ohmic contacts. Further investigations on the dynamics of the metallic atom interchange occurring at metal/metal-oxide interface are required.

5. Experimental Section

The MoO_3 films were deposited via thermal evaporation, using a high purity molybdenum trioxide powder (Sigma-Aldrich, 99.97% trace metals basis). All films were grown in high vacuum conditions (base pressure 5×10^{-5} mbar) on different substrates. The deposition rate was kept as low as 1.5–2 Å s^{-1}. The film thickness was measured with a quartz crystal microbalance. The MoO_3 film was deposited on three different substrates that is, 0.01 mm thick copper foil (from Goodfellow, purity 99.9%), 0.01 thick aluminum foil (Goodfellow, purity 99%), and silicon (100) wafers. The substrates were cleaned in acetone and sonicated in ethanol prior to the deposition. Thermal treatments were performed in a stainless steel chamber with controlled ambient.[46] Films underwent three different thermal treatments. In vacuum, keeping the chamber pressure lower than 10^{-4} mbar. In a nitrogen (N_2) atmosphere filling the chamber with 20 mbar of air partial pressure, and in a N_2 filled chamber but with 50 mbar of air partial pressure. To rule out possible insertion of nitrogen atoms into the structure of the growth films, an in situ annealing check was performed in pure N_2 ambient. The measurements ruled out the presence of N_2 in the structure of the films and/or formation of the N—Mo bonds. Samples were treated with a thermal annealing procedure, for which they reached their final temperature of 410 °C by 5 °C min^{-1} heating rate and then, after being kept at constant temperature for 10 min, were rapidly cooled down to room temperature. Monocrystalline flakes, exfoliated and deposited on a copper substrate (see Supporting Information), were also subjected to the same thermal treatment in 50 mbar of air partial pressure. A second set of samples (indicated in the text by "R") had been subjected to a faster heating rate, reaching the same final temperature by 20 °C min^{-1}, than kept at constant temperature for 5 min. SEM images were collected using "ZEISS SIGMA 300 FESEM", with maximum resolution of 1.2 nm at 15 kV. AFM images were obtained with a "Nano-Observer Atomic Force Microscope" equipped with the controller operated in resonant mode; silicon probes with 10 nm tip radius and nominal cantilever force constant were used. Micro Raman spectroscopy was carried out using a green laser ($\lambda = 532$ nm) with a controlled laser power.[47] All spectra were acquired 30 times with an acquisition time of 30 s, using a 1800 ll mm^{-1} grating. The measurements were repeated on several points to achieve an average result on the sample, while the laser power was optimized to avoid laser crystallization effects (see Supporting Information). In situ measurements were carried out during the thermal treatments with the 5 °C min^{-1} rate . In the in situ set up, the intensity of the peaks was attenuated and hence the 600 lines/mm grating was used in this case. Hence, a loss of the resolution and a broadening of the peaks are expected. Transport measurements were performed with the two-point probe method, both on as deposited film as well as after thermal treatments. The ohmic contacts were realized with the deposition of 60 nm of silver contacts over the film's surface. Two probes were then fixed on the contacts with a gold-based glue and connected to the acquisition system. The resistance of the samples was measured from the *I–V* characteristics at room temperature.

Conflict of Interest

The authors declare no conflict of interest.

Data Availability Statement

The data that support the findings of this study are available in the supplementary material of this article.

[1] M. Vasilopoulou, A. M. Douvas, D. G. Georgiadou, L. C. Palilis, S. Kennou, L. Sygellou, A. Soultati, I. Kostis, G. Papadimitropoulos, D. Davazoglou, P. Argitis, *J. Am. Chem. Soc.* **2012**, *134*, 16178.

[2] T. Ivanova, K. Gesheva, G. Popkirov, M. Ganchev, E. Tzvetkova, *Mater. Sci. Eng., B* **2005**, *119*, 232.

[3] A. Marcelli, S. Bruno, G. Castorina, W. Xu, S. Sarti, F. Monforte, G. Cibin, *Condens. Matter* **2017**, *2*, 18.

[4] A. D'Elia, S. J. Rezvani, A. Cossaro, M. Stredansky, C. Grazioli, B. W. Li, C. W. Zou, M. Coreno, A. Marcelli, *J. Supercond. Novel Magn. 33*, 2383, https://doi.org/10.1007/s10948-019-05378-0.

[5] D. O. Scanlon, G. W. Watson, D. J. Payne, G. R. Atkinson, R. G. Egdell, D. S. L. Law, *J. Phys. Chem. C* **2010**, *114*, 4636.

[6] E. D. Hanson, L. Lajaunie, S. Hao, B. D. Myers, F. Shi, A. A. Murthy, C. Wolverton, R. Arenal, V. P. David, *Adv. Funct. Mater.* **2017**, *27*, 1605380.

[7] S. Cong, A. Hadipour, T. Sugahara, T. Wei, J. Jiu, S. Ranjbar, Y. Hirose, M. Karakawa, S. Nagao, T. Aernouts, K. Suganuma, *J. Mater. Chem. C* **2017**, *5*, 889.

[8] O. de Melo, Y. González, A. Climent-Font, P. Galán, A. Ruediger, M. Sánchez, C. Calvo-Mola, G. Santana, V. Torres-Costa, *J. Phys.: Condens. Matter* **2019**, *31*, 295703.

[9] K. Crowley, G. Ye, R. He, K. Abbasi, X. P. A. Gao, *ACS Appl. Nano Mater.* **2018**, *1*, 6407.

[10] M. Kröoger, S. Hamwi, J. Meyer, T. Riedl, W. Kowalsky, A. Kahn, *Appl. Phys. Lett.* **2009**, *95*, 123301.

[11] S. Shen, X. Zhang, X. Cheng, Y. Xu, S. Gao, H. Zhao, X. Zhou, L. Huo, *ACS Appl. Nano Mater.* **2019**, *2*, 8016.

[12] T. Jaouen, G. Jézéquel, G. Delhaye, B. Lépine, P. Turban, P. Schieffer, *Appl. Phys. Lett.* **2010**, *97*, 232104.

[13] L. Qiu, K. Chen, D. Yang, M. Zhang, X. Hao, W. Li, W. Wang, *Mater. Sci. Semicond. Process.* **2021**, *122*, 105475.

[14] H. Lin, W. Xia, H. N. Wu, C. W. Tang, *Appl. Phys. Lett.* **2010**, *97*, 123504.

[15] M. Zhang, L. Qiu, W. Li, J. Zhang, L. Wu, L. Feng, *Mater. Sci. Semicond. Process.* **2018**, *86*, 49.

[16] S. Macis, C. Aramo, C. Bonavolontá, G. Cibin, A. D'Elia, I. Davoli, M. De Lucia, M. Lucci, S. Lupi, M. Miliucci, A. Notargiacomo, C. Ottaviani, C. Quaresima, M. Scarselli, J. Scifo, M. Valentino, P. De Padova, A. Marcelli, *J. Vac. Sci. Technol., A* **2019**, *37*, 021513.

[17] S. Macis, L. Tomarchio, S. Tofani, S. Javad Rezvani, L. Faillace, S. Lupi, A. Irizawa, A. Marcelli, *Condens. Matter* **2020**, *5*, 16.

[18] M. T. Greiner, L. Chai, M. G. Helander, W.-M. Tang, Z. Lu, *Adv. Funct. Mater.* **2013**, *23*, 215.

[19] M. Dieterle, G. Weinberg, G. Mestl, *Phys. Chem. Chem. Phys.* **2002**, *4*, 812.

[20] S. Macis, J. Rezvani, I. Davoli, G. Cibin, B. Spataro, J. Scifo, L. Faillace, A. Marcelli, *Condens. Matter* **2019**, *4*, 1.

[21] S.-H. Lee, M.-J. Seong, C. Tracy, A. Mascarenhas, J. Pitts, S. Deb, *Solid State Ionics* **2002**, *147*, 129.

[22] K. Ajito, L. A. Nagahara, D. A. Tryk, K. Hashimoto, A. Fujishima, *J. Phys. Chem.* **1995**, *99*, 16383.

[23] H. Yang, R. Jenkins, R. Thompson, R. Downs, S. Evans, E. Bloch, *Am. Mineral.* **2012**, *97*, 197.

[24] M. Camacho-López, L. Escobar-Alarcón, M. Picquart, R. Arroyo, G. Córdoba, E. Haro-Poniatowski, *Opt. Mater.* **2011**, *33*, 480.

[25] M. Dieterle, G. Mestl, *Phys. Chem. Chem. Phys.* **2002**, *4*, 822.

[26] D. Sundeep, A. Krishna, R. Ravikumar, T. Kumar, S. Ephraim, Y. Pavan, *Int. Nano Lett.* **2016**, *6*, 119.

[27] M. Nagano, M. Greenblatt, *J. Non-Cryst. Solids* **1988**, *101*, 255.

[28] S. Touihri, A. Arfaoui, Y. Tarchouna, A. Labidi, M. Amlouk, J. Bernede, *Appl. Surf. Sci.* **2017**, *394*, 414.

[29] E. Lalik, W. I. F. David, P. Barnes, J. F. C. Turner, *J. Phys. Chem. B* **2001**, *105*, 9153.

[30] L. Wang, G.-H. Zhang, K.-C. Chou, *Int. J. Refract. Met. Hard Mater.* **2016**, *57*, 115.

[31] H. Solache-Carranco, G. Juarez-Diaz, M. Galvan-Arellano, J. Martinez-Juarez, G. Romero-Paredes R, R. Pena-Sierra, in *2008 5th Int. Conf. on Electrical Engineering, Computing Science, and Automatic Control*, IEEE, Piscataway, NJ **2008**, pp. 421–424.

[32] I. de Castro Silva, A. C. Reinaldo, F. A. Sigoli, I. O. Mazali, *RSC Adv.* **2020**, *10*, 18512.

[33] P. Pagare, A. Torane, *Microchim. Acta* **2016**, *183*, 2983.

[34] L. Debbichi, M. C. Marco de Lucas, J. F. Pierson, P. Krüger, *J. Phys. Chem. C* **2012**, *116*, 10232.

[35] M. Rellán-Piñeiro, N. López, *J. Phys. Chem. Lett.* **2018**, *9*, 2568.

[36] R. Burch, *J. Chem. Soc., Faraday Trans. 1* **1978**, *74*, 2982.

[37] E. R. S. Winter, *J. Chem. Soc. A* **1968**, 2889.

[38] E. Lalik, *Catal. Today* **2011**, *169*, 85.

[39] P. L. Gai-Boyes, *J. Solid State Chem.* **1993**, *104*, 119.

[40] E. Soltys, K. K. Urazov, T. S. Kharlamova, O. V. Vodyankina, *Kinet. Catal.* **2018**, *59*, 58.

[41] J. Haber, T. Machej, L. Ungier, J. Ziolkowski, *J. Solid State Chem.* **1978**, *25*, 207.

[42] M. Saghafi Yazdi, M. Noghani, A. Najari, *J. Ultrafine Grained Nanostruct. Mater.* **2018**, *51*, 153.

[43] M. T. Greiner, L. Chai, M. G. Helander, W.-M. Tang, Z.-H. Lu, *Adv. Funct. Mater.* **2012**, *22*, 4557.

[44] N. Miyata, T. Suzuki, R. Ohyama, *Thin Solid Films* **1996**, *281-282*, 218.

[45] L. De Los Santos Valladares, D. H. Salinas, A. B. Dominguez, D. A. Najarro, S. Khondaker, T. Mitrelias, C. Barnes, J. A. Aguiar, Y. Majima, *Thin Solid Films* **2012**, *520*, 6368.

[46] F. Paparoni, S. J. Rezvani, *Optical Annealing Chamber for In-situ Raman Spectroscopy in Controlled Ambient*, unpublished.

[47] S. J. Rezvani, E. Mijit, A. Di Cicco, *Appl. Phys. Lett.* **2021**, *119*, 053101.